# A Large Eddy Simulation Study of a Quasi-Steady, Stably Stratified Atmospheric Boundary Layer

BRANKO KOSOVIĆ AND JUDITH A. CURRY

*Program in Atmospheric and Oceanic Sciences, University of Colorado, Boulder, Colorado*

(Manuscript received 2 April 1998, in final form 15 January 1999)

ABSTRACT

Using the large eddy simulation (LES) technique, the authors study a clear-air, stably stratified atmospheric boundary layer (ABL) as it approaches a quasi-steady state. The Beaufort Sea Arctic Stratus Experiment (BASE) dataset is used to impose initial and boundary conditions. The authors explore the parameter space of the boundary layer by varying latitude, surface cooling rate, geostrophic wind, inversion strength, and surface roughness. Recognizing the critical dependence of the results of LES on the subgrid-scale (SGS) model, they test and use a nonlinear SGS model, which is capable of reproducing the effects of backscatter of turbulent kinetic energy (TKE) and of the SGS anisotropies characteristic for shear-driven flows. In order to conduct a long-term LES so that an ABL can reach a quasi-steady state, a parallel computer code is developed and simulations with a spatial domain of up to $96^3$ grid points are performed.

The authors analyze the evolution of the mean wind, potential temperature, and turbulence profiles as well as the turbulence budgets. In their simulations, they observe the development of features that are characteristic of a stably stratified ABL: a two-layer ABL structure, an elevated inversion, and an associated inversion wind maxima. Good agreement is found between the LES results and the observations and with Nieuwstadt's analytical model. The authors study the dependence of the boundary layer height on the flow parameters and determine model coefficients for a truncated Zilitinkevich–Mironov model.

## 1. Introduction

Although significant advances in understanding the stable atmospheric boundary layer (ABL) have been achieved in recent years, and a more comprehensive insight is currently emerging [for recent reviews cf. Hunt et al. (1996); and Andreas (1996)], a broad theoretical framework comparable to that for convective ABLs has not yet been developed. The intrinsic unsteadiness of the stable ABL, characterized by the inertial oscillation, intermittent turbulence, and gravity waves, imposes severe restrictions in developing such a framework (e.g., Hunt et al. 1985). These restrictions prompted Hunt (1985) to conclude that the stable ABL is probably too variable to be characterized reliably by typical profiles of the turbulence and mean velocity for general air pollution dispersion calculations. Derbyshire (1995) recently presented a detailed comparison of field measurements and large eddy simulation (LES) results. Although he observed a broad agreement between the structure of observed midlatitude ABLs and LES results, he found that LES results match the idealized theories more closely than do the observations. Derbyshire attributed this to temporal variability and spatial heterogeneity of observed stable ABLs. The variability of observed nocturnal ABLs can also be associated with the inertial oscillation. Since the period of this oscillation decreases with latitude, Businger and Arya (1974) suggested that a stable ABL can reach a quasi-steady state only during the polar night.

A quasi-steady ABL is characterized by a temperature profile changing at a constant rate throughout the ABL while all other mean flow and turbulence properties have reached a steady state. However, due to the the long period of the inertial oscillation as well as the inherent intermittence of a stable ABL, in reality a quasi-steady state is a rare occurrence. Nevertheless, as Derbyshire (1990) recently pointed out, determining the conditions under which stable ABL can be quasi steady presents a large obstacle to theoretical progress in understanding the structure of a stable ABL and its evolution. More detailed knowledge of the equilibrium state of a stable ABL is essential, since it represents a limiting state of any relaxation process.

Significant insight has been gained by numerical studies of stable ABLs using second-order closure (Delage 1974; Wyngaard 1975; Brost and Wyngaard 1978; Zeeman 1979). However, by neglecting small transport terms, a second-order closure effectively reduces to a

*Corresponding author address:* Branko Kosović, Aerospace Engineering Science Department, Campus Box 429, University of Colorado, Boulder, CO 80309.
E-mail: kosovic@cloud.colorado.edu

simple gradient diffusion model. Nieuwstadt (1985) demonstrated that under a few simplifying assumptions such a gradient-diffusion model can be approached analytically. Following the concept of ''z-less'' scaling introduced by Wyngaard (1975), Nieuwstadt (1984) proposed local scaling for turbulence properties in a stable ABL. Although a local scaling hypothesis has been confirmed using experimental observations and numerical simulations of weakly stable ABLs (Nieuwstadt 1984; Derbyshire 1990, 1995; Wyngaard and Kosović 1994) and represents an insightful concept, it is of very limited use in modeling, since it assumes a priori knowledge of turbulent stress and flux profiles. Nieuwstadt's quasi-steady model is applicable to weakly and moderately stable ABLs. In strongly stratified ABLs, Mahrt (1989) observed global intermittence. Kim and Mahrt (1992) proposed a conceptual picture in which a strongly stable ABL can be divided in two regions: a relatively thin layer near the surface, which is characterized by a sustained shear-driven turbulence, and an overlaying layer that is dominated by gravity waves and characterized by weak, globally intermittent turbulence. Derbyshire (1994) assumed that a stable state is not necessarily steady, and performed a stability analysis of a linearized system of equations governing the evolution of the mean shear and the mean temperature gradient.

Using direct Navier–Stokes simulations (DNS) of stably stratified (low Reynolds number), boundary layer flows, Coleman et al. (1992) concluded that in some instances, results of low Reynolds number simulations exhibit Reynolds number independence and thus can be extended to high Reynolds number flows. However, some of the basic flow parameters such as gradient and flux Richardson numbers obtained using DNS exhibit significantly different behavior compared with experimental observations and LES results. Also, due to the presence of viscous stress effects, the inertial oscillation of the wind vector near the ABL top is strongly damped in the DNS, and thus the development of the jet (inversion wind maximum) is strongly suppressed.

Previous numerical studies of ABLs have been focused mostly on LES of a few simple types of homogeneous, canonical boundary layers. In particular, extensive and successful studies have been conducted of convective and neutral boundary layers. However, stable stratification and associated damping of vertical motions in the boundary layer is no less prevalent than convection. Stable conditions are characteristic not only of the nocturnal boundary layer over land but also of warmer air flowing over a cold ocean, as in polar regions. During the polar winter, stable conditions can persist for months, decoupling the surface from conditions in the lower troposphere. Recently, Curry et al. (1996) summarized the observations related to the inversions in the Arctic and concluded that even in summertime stable conditions often extend over several days.

The first LES of a stable boundary layer performed by Mason and Derbyshire (1990) showed that the global statistics obtained from such simulations depend critically on the subgrid-scale (SGS) model used. These simulations also showed that the commonly used linear, Smagorinsky-type SGS models may not be appropriate for simulating stable boundary layers due to the fact that they are absolutely dissipative and as such can cause relaminarization of the flow. To overcome these limitations, Mason and Thompson (1992) developed a stochastic-backscatter model. Using the backscatter model, Brown et al. (1994) repeated and expanded numerical simulations of a stable ABL conducted by Mason and Derbyshire (1990). Brown et al. found that with the backscatter SGS model, the nondimensional shear and the nondimensional potential temperature gradient in the surface layer agree much better with the observations than when the Smagorinsky-type model is used. To perform LES of a stable ABL, Andrén (1995) successfully used the anisotropy SGS model developed by Sullivan et al. (1994). In this paper, we extend these studies to further examine the stable ABL using LES.

The LES of the stable ABL depends critically on the SGS model, so we compare the results obtained using three different SGS models: the linear, Smagorinsky-type SGS model (Moeng 1984); the anisotropy SGS model of Sullivan et al. (1994); and the nonlinear SGS model (Kosović 1997). The nonlinear model was developed to account for the backscatter of energy and anisotropy due to the shear. Both of these effects are present in shear-driven, stably stratified ABLs and are important for the evolution a quasi-steady, stably stratified ABL.

In order to better resolve turbulent scales of motion, the numerical domain size in our simulations will be relatively small and will not be sufficient to resolve large-scale wave motions. We will therefore focus on analysis of boundary layers dominated by turbulence effects. We use the LES technique to study a high-latitude, idealized (homogeneous) stably stratified ABL as it approaches a quasi-steady state.

Although stable cloud-topped ABLs are common in the Arctic and have a profound effect on the thermal budgets affecting climate scales, the first step in our analysis of the stable boundary layer will focus on the clear-air boundary layer. Even though in a clear-air case, longwave radiative effects dominate total cooling in the surface layer and the uppermost ABL layer significantly affecting the surface layer shear and potential temperature gradient, they do not seem to affect bulk boundary layer parameters and turbulent stresses (Garratt and Brost 1981). In the present study, we therefore do not take into consideration radiative effects. We used the Beaufort Sea Arctic Stratus Experiment (BASE) dataset, corresponding to the flight number 7 on 1 October 1994, to impose initial and boundary conditions in order to numerically simulate a clear-air, stably stratified ABL characterized by a moderate surface cooling rate.

In a series of a low-resolution simulations, we explore the parameter space by varying surface cooling rate,

geostrophic wind, latitude, overlaying inversion strength, and surface roughness. We use the results of these simulations to test different hypotheses related to the stable ABL in a quasi-steady state. Our analysis focuses on global characteristics of a quasi-steady, stably stratified ABL structure with the aim of providing a better understanding of the ABL evolution under stable conditions and consequently result in better parameterizations of such ABLs in mesoscale and macroscale models. We analyze the mean wind, potential temperature, and turbulence profiles as well as turbulence budgets related to the high-resolution simulations in section 5. In our simulations, we observed the development of features that are characteristic of a stably stratified ABL: elevated inversions and the associated inversion wind maxima. In section 6, we use LES results to determine model parameters for an ABL height model recently developed by Zilitinkevich and Mirnov (1996). The Zilitinkevich–Mironov model simultaneously accounts for the effects of rotation, surface heat flux, and stability of the overlaying free flow. Finally, we present a summary and our conclusions in section 7.

## 2. Governing equations

Flows in atmospheric boundary layers can be considered incompressible. Thus the resolved momentum conservation equations used in LES have the following form (cf. Moeng 1984):

$$\frac{\partial \tilde{u}_i^r}{\partial t} = -\varepsilon_{ijk}\tilde{u}_j^r\tilde{\omega}_k^r - \frac{1}{\rho}\frac{\partial \tilde{\Pi}^r}{\partial x_i} - \frac{\partial \sigma_{ij}}{\partial x_j} - \frac{g}{T_0}\tilde{\theta}^r\delta_{i3} - 2\varepsilon_{ijk}\zeta_j\tilde{u}_k^r. \quad (1)$$

Here, $\tilde{u}_i^r$ is the resolved (filtered) velocity field, $\tilde{\omega}_k^r$ is the corresponding vorticity, and $\tilde{\Pi}^r$ is the modified resolved pressure field. In the momentum conservation equation, we have accounted for the buoyancy effects via the Boussinesq approximation. The reference temperature is denoted by $T_0$, while $\tilde{\theta}^r$ denotes resolved potential temperature and $\zeta_j$ is the earth's rotation rate vector. The resolved velocity field, $\tilde{u}_i^r$, is solenoidal:

$$\frac{\partial \tilde{u}_i^r}{\partial x_i} = 0. \quad (2)$$

The potential temperature conservation equation is

$$\frac{\partial \tilde{\theta}^r}{\partial t} + \tilde{u}_j^r\frac{\partial \tilde{\theta}^r}{\partial x_j} = -\frac{\partial \vartheta_j}{\partial x_j}. \quad (3)$$

In (1)–(3), the superscript $r$ denotes resolved fields obtained by filtering total fields so that any filtered field $\tilde{f}^r$ is defined as

$$\tilde{f}^r(\mathbf{x}) = \int_{\mathcal{V}} G(\mathbf{x} - \boldsymbol{\xi})\tilde{f}(\boldsymbol{\xi})\, d\xi. \quad (4)$$

Here, $G(\mathbf{x})$ is a filter function. In all our simulations, we use a wave cutoff filter in the horizontal plane, and no explicit filtering is defined for the vertical direction. In (1), $\sigma_{ij}$ is the anisotropic component of the SGS stress tensor $\tau_{ij}$:

$$\sigma_{ij} = \tau_{ij} - \frac{1}{3}\tau_{kk}. \quad (5)$$

The SGS stress $\tau_{ij}$ is defined as

$$\tau_{ij} = (\tilde{u}_i\tilde{u}_j)^r - \tilde{u}_i^r\tilde{u}_j^r = (\tilde{u}_i^r\tilde{u}_j^r)^r - \tilde{u}_i^r\tilde{u}_j^r + [(\tilde{u}_i^r\tilde{u}_j^s + \tilde{u}_i^s\tilde{u}_j^r) + \tilde{u}_i^s\tilde{u}_j^s]^r. \quad (6)$$

The isotropic component of the SGS stress, $\frac{1}{3}\tau_{kk}$, is added to the pressure, $p$. The SGS flux, $\vartheta_j$, is defined as

$$\vartheta_j = (\tilde{\theta}\tilde{u}_j)^r - \tilde{\theta}^r\tilde{u}_j^r = (\tilde{\theta}^r\tilde{u}_j^r)^r - \tilde{\theta}^r\tilde{u}_j^r + [(\tilde{\theta}^r\tilde{u}_j^s + \tilde{\theta}^s\tilde{u}_j^r) + \tilde{\theta}^s\tilde{u}_j^s]^r. \quad (7)$$

In (6)–(7), the superscript s denotes the subgrid fields, which are defined as the difference between the total and filtered fields:

$$\tilde{u}_i^s = \tilde{u}_i - \tilde{u}_i^r \quad \text{and} \quad \tilde{\theta}^s = \tilde{\theta} - \tilde{\theta}^r. \quad (8)$$

The modified resolved pressure, defined as

$$\tilde{\Pi}^r = \tilde{p}^r + \frac{1}{2}\tilde{u}_l^r\tilde{u}_l^r + \frac{1}{3}\tau_{kk}, \quad (9)$$

is determined by taking the divergence of (1) and solving the resulting Poisson equation:

$$\frac{\partial^2 \tilde{\Pi}^r}{\partial x_i \partial x_i} = -\varepsilon_{ijk}\frac{\partial \tilde{u}_j^r\tilde{\omega}_k^r}{\partial x_i} - \frac{\partial^2 \sigma_{ij}}{\partial x_j \partial x_i} - \frac{g}{T_0}\frac{\partial \tilde{\theta}^r}{\partial x_3} - 2\varepsilon_{ijk}\frac{\partial \zeta_j\tilde{u}_k^r}{\partial x_i}. \quad (10)$$

## 3. Subgrid-scale models

The effects of the SGS model in simulations of stable boundary layers are more significant than in convective or neutral cases because a greater portion of turbulent kinetic energy and temperature variance is not resolved due to the small scale of the eddies. Mason and Thompson (1990) showed that under such conditions, it is important to account for the effects of the backscatter of energy from small, unresolved scales toward large, resolved scales of motion. In addition, Sullivan et al. (1994) showed that in the surface layers of a stable ABL, a subgrid-stress model must account for anisotropy due to the shear. Therefore, they developed the anisotropy model. To account for both the effects of the backscatter as well as the shear, Kosović (1997) developed a nonlinear SGS model. In this study, we compare the performance of the nonlinear SGS model in LES of stably stratified ABL to that of the commonly used linear, Smagorinsky-type model (Moeng 1984) and the anisotropy model (Sullivan et al. 1994) in simulating a stable ABL. After confirming that its performance is satisfactory, we

used only the nonlinear SGS model to study a stably stratified ABL as it approaches a quasi-steady state.

The nonlinear SGS stress model, $M_{ij}$ (Kosović 1997), is defined as

$$M_{ij} = -C_e\Delta\left\{2(e^r_{\rm sgs})^{1/2}S_{ij} + \left(\frac{27}{8\pi}\right)^{1/3}C_s^{2/3}\Delta \times\left[C_1\left(S_{ik}S_{kj} - \frac{1}{3}S_{mn}S_{nm}\delta_{ij}\right) + C_2(S_{ik}\Omega_{kj} - \Omega_{ik}S_{kj})\right]\right\}. \quad (11)$$

Here, $S_{ij}$ and $\Omega$ are strain rate tensor and rotation rate tensor, respectively, defined as

$$S_{ij} = \frac{1}{2}\left(\frac{\partial\tilde{u}^r_i}{\partial x_j} + \frac{\partial\tilde{u}^r_j}{\partial x_i}\right) \quad \text{and} \quad \Omega_{ij} = \frac{1}{2}\left(\frac{\partial\tilde{u}^r_i}{\partial x_j} - \frac{\partial\tilde{u}^r_j}{\partial x_i}\right) \quad (12)$$

The length scale, $\Delta$, is related to the grid-cell size as follows:

$$\Delta = (\Delta x\Delta y\Delta z)^{1/3}. \quad (13)$$

Since reducing the length scale below the grid-cell size may result in a spurious high wavenumber noise, we follow Canuto and Cheng (1997) and use the grid-cell size as the characteristic length scale, regardless of the stability conditions. The model parameter, $C_e$, can be related to the Smagorinsky parameter:

$$C_e = \pi^{1/3}\left(\frac{2}{3C_K}\right)^{1/2}C_s^{4/3} = \left(\frac{8\pi}{27}\right)^{1/3}C_s^{4/3}. \quad (14)$$

Here, $C_K$ denotes the Kolmogorov constant for which we assume the experimentally determined value $C_K \approx 1.5$. Unlike in a linear, Smagorinsky-type SGS model, the Smagorinsky parameter, $C_s$, is not a constant, but is a function of the backscatter parameter:

$$C_s = \left[\frac{8(1 + C_b)}{27\pi^2}\right]^{1/2}. \quad (15)$$

The backscatter parameter is defined as the ratio of the rate of the backscatter of turbulent kinetic energy (TKE) to the dissipation rate:

$$\langle\epsilon\rangle = T(k_c) = [C_f(k_c) - C_b(k_c)]\langle\epsilon\rangle \quad \forall k_c \text{ in inertial range.} \quad (16)$$

Here, $\langle\cdot\rangle$ denotes an ensemble average; $\epsilon$ is the dissipation rate; $T(k_c)$ is the inertial transfer rate through the cutoff wavenumber, $k_c$; and $C_f$ is the coefficient of the forward scatter—a ratio of the rate of the forward scatter of energy to the dissipation rate. When using an absolutely dissipative SGS model, the backscatter parameter is implicitly set to zero. By conducting numerical experiments, Kosović (1997) found that the optimal value of the backscatter parameter is $C_b = 0.36$, which is in a agreement with the theoretical prediction and the DNS results.

The nonlinear model parameters, $C_1$ and $C_2$, are determined so that the model provides correct energy transfer and captures the normal stress effects observed in homogeneous, sheared flows. Kosović found that parameter $C_1$ can be related to the backscatter parameter and the skewness function:

$$C_1 = \frac{960^{1/2}C_b}{7(1 + C_b)\mathcal{S}(k_c)}. \quad (17)$$

Here, $\mathcal{S}(k_c)$ is the resolved velocity derivative skewness function:

$$\mathcal{S}(k_c) = -\frac{\left\langle\left(\frac{\partial u^r_1}{\partial x_1}\right)^3\right\rangle}{\left\langle\left(\frac{\partial u^r_1}{\partial x_1}\right)^2\right\rangle^{3/2}}. \quad (18)$$

The skewness function is a function of the cutoff wavenumber only. However, when the cutoff wavenumber is in the inertial subrange, the skewness function assumes a value comparable to that of the skewness factor, $s$, based on the total velocity field. Therefore, we set the skewness function to an experimentally determined value, $\mathcal{S}(k_c) = 0.5$. In contrast to the linear SGS term, which on average contributes to the forward cascade of energy, the nonlinear term on average contributes to the backscatter of energy. The second model parameter, $C_2$, cannot be determined from the TKE considerations, since the terms involving the rotation rate tensors do not contribute to the TKE balance. However, in order to reproduce the observed normal stress effects, the model parameter $C_2$ should be equal to the parameter $C_1$ (Kosović 1997).

We are concerned with inhomogeneous, high Reynolds number boundary layer flows, and therefore, we use the SGS TKE equation (19) to determine the velocity scale, $(e^r_{\rm sgs})^{1/2}$, for the transport coefficient. This is analogous to Lilly's (1967) ''turbulent energy method.'' In this case, an additional partial differential equation for the SGS kinetic energy solved along with the Navier–Stokes equations is

$$\frac{\partial e^r_{\rm sgs}}{\partial t} + \left[u^r_j\frac{\partial e^r_{\rm sgs}}{\partial x_j}\right]^r = -\tau_{ij}\frac{\partial u^r_i}{\partial x_j} + \frac{g}{T_0}(u^s_3\theta^s)^r - \frac{\partial[u^s_i(e_{\rm sgs} + p^s/\rho)]^r}{\partial x_i} - \epsilon. \quad (19)$$

The SGS turbulent kinetic energy $e_{\rm sgs}$ is defined as

$$e_{\rm sgs} = \frac{1}{2}[(\tilde{u}_l\tilde{u}_l)^r - \tilde{u}^r_l\tilde{u}^r_l]. \quad (20)$$

In (19), $\epsilon$ denotes the dissipation rate, which has to be modeled along with the transport term (the third on the

right-hand side of the equation). These terms are modeled in the same way as in Moeng (1984):

$$[u_i^s(e_{\text{sgs}} + p^s/\rho)]^r = -2C_e\Delta(e_{\text{sgs}}^r)^{1/2}\frac{\partial e_{\text{sgs}}^r}{\partial x_i} \quad (21)$$

$$\epsilon = \frac{C_e(e_{\text{sgs}}^r)^{3/2}}{l_\epsilon} \quad (22)$$

Unlike the mixing length in (11), the dissipation length scale, $l_\epsilon$, in (22) depends on the stability conditions. While in a Reynolds stress model the mixing length scale, $\Delta$, and the dissipation length scale, $l_\epsilon$, are directly related, in LES this is not the case. The question of proper dissipation length scales for second-order Reynolds stress closures and for LES of stably stratified flows was discussed by Schumann (1991). Focusing on the correct limiting behavior for the vanishing shear and temperature gradient, we developed a simple algebraic relation for the dissipation length scale:

$$l_\epsilon = \left[\frac{1}{\Delta^2} + \frac{1}{l_n^2} + \frac{1}{l_s^2}\right]^{-(1/2)}. \quad (23)$$

Functional dependence of the dissipation length scale on the local resolved temperature gradient (Brunt–Väisälä frequency) and on the local shear is similar to that proposed by Canuto and Cheng (1997). Here, $l_n$ and $l_s$ are SGS buoyancy and shear length scales, respectively. These length scales are defined as

$$l_n = 0.76\frac{\sqrt{e_{\text{sgs}}}}{N} \quad \text{and} \quad l_s = 2.76\frac{\sqrt{e_{\text{sgs}}}}{S}. \quad (24)$$

Here, $N$ denotes Brunt–Väisälä frequency, $N = \sqrt{g/T_0(\partial\theta^r/\partial z)}$, while $S$ denotes the magnitude of the resolved shear, $S = \sqrt{(\partial u^r/\partial z)^2 + (\partial v^r/\partial z)^2}$. The buoyancy length scale was defined as analogous to Brost and Wyngaard (1978). This length scale is commonly used in LES (e.g., Deardorff 1980; Moeng 1984). The shear length scale was defined as analogous to Hunt et al (1988), who argued that a more proper dissipation length scale for a shear-driven stable ABL should depend on the shear magnitude instead of the temperature gradient. Notice that in the case of isotropic turbulence, that is, in the absence of shear or temperature gradient, the dissipation length scale would correspond to the grid size. However, in the anisotropic case, where turbulence is produced or destroyed by the action of a shear or temperature gradient, the dissipation length scale is smaller than the grid size. We should point out that the relation (23) does not result in an increasing length scale with increased stability.

We use a simple gradient diffusion model for the SGS heat fluxes (Deardorff 1980):

$$\vartheta_j = -K_e\frac{\partial\tilde{\theta}^r}{\partial x_j}. \quad (25)$$

Eddy diffusivity, $K_e$, is related to the eddy viscosity, as follows:

$$K_e = \frac{C_e\Delta(e_{\text{sgs}}^r)^{1/2}}{\text{Pr}_{\text{sgs}}}. \quad (26)$$

Here, $\text{Pr}_{\text{sgs}}$ is the SGS turbulent Prandtl number. We chose the mixing length in (11) to be the grid-size $\Delta$, and therefore following Moeng (1984), the SGS turbulent Prandtl number is implicitly set to ⅓.

When the simple gradient-diffusion model for the potential temperature SGS flux is used along with the linear, Smagorinsky-type SGS stress model, erroneous mean potential temperature gradient profiles are obtained. Mason and Thompson (1992) and Brown et al. (1994) therefore used the backscatter concept in modeling the SGS potential temperature flux. However, Sullivan et al. (1994) found that no adjustment of the SGS flux model was necessary as long as the SGS stress model used in LES produces correct mean shear profiles.

## 4. Large eddy simulation cases

To conduct the simulations, we integrated Eqs. (1), (2), and (3) using the algorithm developed by Moeng (1984) with the time integration performed using the third-order Runge–Kutta scheme. The algorithm was coded in Fortran 77 and parallelized using Message Passing Interface (MPI). The code was executed on the Cray T3E at the Arctic Region Supercomputing Center.

We performed a number of low-resolution simulations using $40^3$ grid points and a selected set of a medium-resolution $64^3$ simulations. The initial conditions, surface cooling rate, and the inversion strength for these simulations were based on the measurements made during BASE on 1 October 1994 from flight number 7. We used the observations made over the Arctic ocean because conditions that persist over sea ice, which include stable stratification, a short inertial oscillation period, and sufficiently strong winds, are conducive to the development of quasi-steady, stably stratified ABLs in the absence of mesoscale effects and surface inhomogeneities. To be able to compare the simulation results with Nieuwstadt's analytical forms of temperature, wind, temperature flux, and turbulent stress profiles of the quasi-steady stable ABL, as the lower boundary condition in all the simulations we specified the surface cooling rate instead of specifying the surface flux.

In the baseline simulation, NLB, the latitude was 73°N, the geostrophic wind was set to 8 m $s^{-1}$, the surface cooling rate was 0.25 K $h^{-1}$, the overlying inversion strength was 0.01 K $m^{-1}$, and the surface roughness was 0.1 m. The baseline case roughness length is higher than the typical roughness length over sea ice in the Arctic ocean. However, due to the limitations of LES resolution, using a significantly lower roughness length would result in an underresolved surface layer. In additonal simulations, we varied the basic parameters: geostrophic wind (NL05GW and NL11GW), cooling rate (NL05CR and NL10CR), latitude (NL45LA and NL22LA), inversion strength (NL00IN and NL20IN),

TABLE 1. Stable atmospheric boundary layer, large eddy simulation cases.

| Run | Resolution (domain size) | Latitude (°N) | Geostrophic wind ($m\ s^{-1}$) | Surface cooling rate ($K\ h^{-1}$) | Inversion strength ($K\ m^{-1}$) | Surface roughness (m) |
|---|---|---|---|---|---|---|
| LB | $40^3$ | 73 | 8 | 0.25 | 0.01 | 0.10 |
| AB | $40^3$ | 73 | 8 | 0.25 | 0.01 | 0.10 |
| NLB | $40^3$ | 73 | 8 | 0.25 | 0.01 | 0.10 |
| NL45LA | $40^3$ | 45 | 8 | 0.25 | 0.01 | 0.10 |
| NL22LA | $40^3$ | 22 | 8 | 0.25 | 0.01 | 0.10 |
| NL05GW | $40^3$ | 73 | 5 | 0.25 | 0.01 | 0.10 |
| NL11GW | $40^3$ | 73 | 11 | 0.25 | 0.01 | 0.10 |
| NL05CR | $40^3$ | 73 | 8 | 0.50 | 0.01 | 0.10 |
| NL10CR | $40^3$ | 73 | 8 | 1.00 | 0.01 | 0.10 |
| NL00IN | $40^3$ | 73 | 8 | 0.25 | 0.0 | 0.10 |
| NL20IN | $40^3$ | 73 | 8 | 0.25 | 0.02 | 0.10 |
| NL05SR | $40^3$ | 73 | 8 | 0.25 | 0.01 | 0.05 |
| NL20SR | $40^3$ | 73 | 8 | 0.25 | 0.01 | 0.20 |
| NLMRB | $64^3$ | 73 | 8 | 0.25 | 0.01 | 0.10 |
| NLMR45LA | $64^3$ | 45 | 8 | 0.25 | 0.01 | 0.10 |
| NLMR22LA | $64^3$ | 22 | 8 | 0.25 | 0.01 | 0.10 |
| NLMR05GW | $64^3$ | 73 | 5 | 0.25 | 0.01 | 0.10 |
| NLMR11GW | $64^3$ | 73 | 11 | 0.25 | 0.01 | 0.10 |
| NLMR05CR | $64^3$ | 73 | 8 | 0.50 | 0.01 | 0.10 |
| NLMR10CR | $64^3$ | 73 | 8 | 1.00 | 0.01 | 0.10 |
| NLHRB | $96^3$ | 73 | 8 | 0.25 | 0.01 | 0.10 |

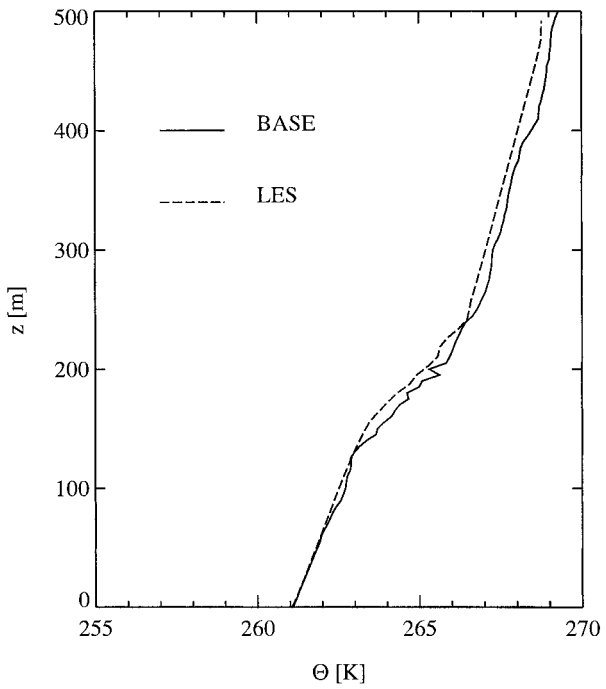


FIG. 1. The potential temperature profile after 8 h of LES compared with the profile observed during flight number 7 of BASE. Solid line, BASE profile; dashed line, LES profile.

and surface roughness (NL05SR and NL20SR). Since the preliminary anlaysis suggested that the first three parameters have a more significant effect on the stable ABL evolution, we performed a set of $64^3$ simulations varying these parameters only (geostrophic wind—NLMR05GW and NLMR11GW, cooling rate—NLMR05CR and NLMR10CR, and latitude—NLMR45LA and NLMR22LA). For all the LES cases, basic simulation parameters are summarized in Table 1.

The potential temperature profile was initialized so that it could develop into the observed profile after several hours of simulation. The initial surface temperature was set at 261 K. While we imposed a shallow mixed layer, a weak inversion was specified above 100 m in all the simulations except the NL00IN case. The initial wind profile was a simple parabolic profile in the streamwise direction, within the first 125 m above the ground level and the constant wind speed equal to the geostrophic wind speed above 125 m. Initially, the cross-stream velocity was equal to zero throughout the boundary layer. We chose to specify such an initial wind profile in order to be able to follow the development of the Ekman spiral and the associated inversion wind maximum. In Fig. 1, the potential temperature profile observed during BASE flight number 7 is compared with the corresponding profile after 8 h of physical time from the NLMR05CR LES case. The upper boundary condition was a radiative boundary condition, permitting internal gravity waves to propagate through the upper boundary (Klemp and Duran 1983). The initial wind, potential temperature, and subgrid kinetic energy pro-

TABLE 2. Initial velocity, potential temperature, and SGS TKE profiles set to $V = 0$ m s$^{-1}$ throughout the ABL. For $z > 250$ m, the mean stream-wise velocity is $U = U_g = 8$ m s$^{-1}$, the mean cross-stream velocity is $V = 0$ m s$^{-1}$, the potential temperature is $\Theta = 266.5 + 0.01(z - 250)$, and the SGS TKE is $\langle e_{sgs} \rangle = 0$.

| Height (m) | $U$ (m s$^{-1}$) | $V$ (m s$^{-1}$) | $\theta$ (K) | SGS TKE (m$^2$ s$^{-2}$) |
|---|---|---|---|---|
| 6.25 | 3.32 | 0.0 | 265.0 | 0.365 |
| 18.75 | 4.42 | 0.0 | 265.0 | 0.295 |
| 31.25 | 5.16 | 0.0 | 265.0 | 0.245 |
| 43.75 | 5.77 | 0.0 | 265.0 | 0.205 |
| 56.25 | 6.30 | 0.0 | 265.0 | 0.175 |
| 68.75 | 6.74 | 0.0 | 265.0 | 0.145 |
| 81.25 | 7.11 | 0.0 | 265.0 | 0.120 |
| 93.75 | 7.42 | 0.0 | 265.0 | 0.100 |
| 106.25 | 7.65 | 0.0 | 265.1 | 0.085 |
| 118.75 | 7.82 | 0.0 | 265.2 | 0.070 |
| 131.25 | 7.93 | 0.0 | 265.3 | 0.055 |
| 143.75 | 7.99 | 0.0 | 265.4 | 0.045 |
| 156.25 | 8.0 | 0.0 | 265.6 | 0.035 |
| 168.75 | 8.0 | 0.0 | 265.7 | 0.025 |
| 181.25 | 8.0 | 0.0 | 265.8 | 0.020 |
| 193.75 | 8.0 | 0.0 | 265.9 | 0.015 |
| 206.25 | 8.0 | 0.0 | 266.1 | 0.010 |
| 218.75 | 8.0 | 0.0 | 266.2 | 0.005 |
| 231.25 | 8.0 | 0.0 | 266.3 | 0.005 |
| 243.75 | 8.0 | 0.0 | 266.4 | 0.005 |

files for low-resolution simulations are tabulated in Table 2. For the medium- and the high-resolution simulations, the initial profiles are obtained by interpreting the values given in Table 2 using cubic splines.

In all simulations, the domain size was 600 × 400 × 500 m in $x$, $y$, and $z$ directions, respectively, the same as in Andrén (1994). The domain size in our simulations was not sufficient to resolve the long wavelength gravity waves observed above the ABL during BASE. Thus, we were not able to study possible gravity wave–turbulence interactions. However, observational evidence suggests that in weakly and moderately stable ABLs dominated by sustained turbulence, gravity wave effects are not significant. We therefore focus our attention on such weakly and moderately stable ABLs. Also, we do not carry out a detailed spectral analysis, since such analysis should include possible gravity wave effects and would require a much larger domain size and a proportionally larger number of grid points in order to resolve both long gravity waves and small turbulent scales. Such analysis and simulations are beyond the scope of the present study and will be undertaken in the future.

All of the simulations corresponding to 73°N latitude were carried out for 12 h of physical time. Due to the longer period of the inertial oscillation at lower latitudes, the 45°N latitude case was integrated for 16 h, and the 22°N latitude case was integrated for 24 h of physical time. All the simulation times correspond to approximately 6$tf$ nondimensional time units where $f$ is the Coriolis parameter.

The mean and turbulence profiles and budgets were computed averaging over the last 2 h of physical time

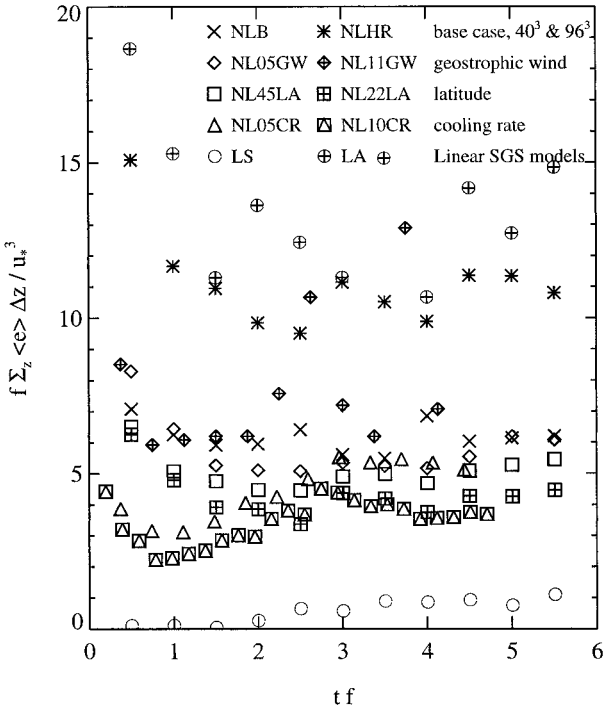


FIG. 2. Iteration history of the normalized TKE, $f \Sigma_z \langle e \rangle \Delta z / u_*$, as a function of the nondimensional time, $tf$, from different LES runs. Symbols represent 1-h averages. Crosses, base cases NLB; stars, high-resolution base case NLHRB; diamonds, geostrophic wind 5 m s$^{-1}$, case NL05GW; crossed diamonds, geostrophic wind 11 m s$^{-1}$, case NL11GW; squares, latitude 45°N, case NL45LA; crossed squares, latitude 22°N, case NL22LA; triangles, cooling rate 0.5 K h$^{-1}$, case NL05CR; boxed triangles, cooling rate 1.0 K h$^{-1}$, case NL10CR; circles, linear, Smagorinsky-type SGS model, base case LS; crossed circles, linear, anisotropy SGS model, base case LA.

of a respective simulation. In all of the low-resolution simulations, a large fraction of the temperature variance, temperature flux, and stress are unresolved and therefore represented by a subgrid model despite the fact that the grid-cell size is relatively small. We therefore performed high-resolution simulations of the baseline case, labeled NLHRB, using only the nonlinear SGS model and $96^3$ grid points. This simulation was performed on 32 Cray-T3E processors in parallel and enabled us to evaluate the grid-scale dependence of the results. The computational intensity of such a long-term simulation was a prohibitive factor that precluded us from performing more high-resolution simulations.

In all the LES cases described above, we used the nonlinear SGS model described in the previous section. To test the SGS model effects, we also used the linear, Smagorinsky-type model and the anisotropy model for $40^3$ baseline case simulations labeled LB and AB, respectively. The linear, Smagorinsky-type model was the same as the one used by Moeng (1984), while the anisotropy model was developed by Sullivan et al. (1994). The evolution history of the total TKE for all the LES cases is presented in Fig. 2. It is obvious that the linear, Smagorinsky-type SGS model is too dissipative, re-

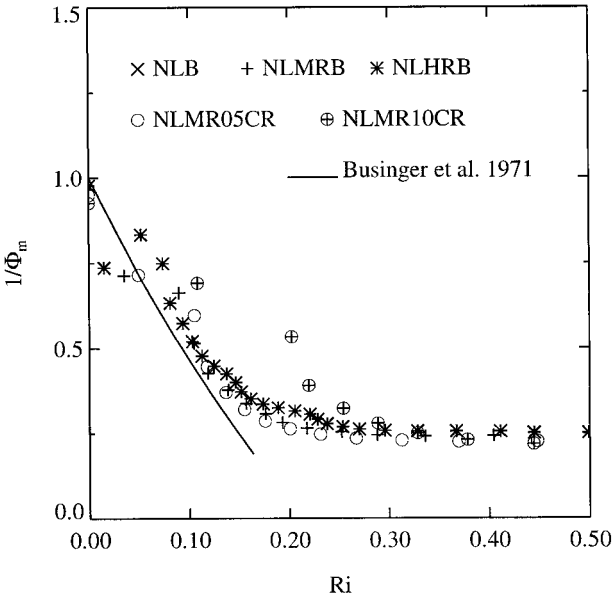


FIG. 3. Nondimensional shear as a function of the gradient Richardson number. Crosses, base cases NLMRB; pluses, medium resolution base case NLMRB; stars, high-resolution base case NLHRB; circles, cooling rate 0.5 K $h^{-1}$, case NLMR05CR; crossed circles, cooling rate 1.0 K $h^{-1}$, case NLMR10CR; solid line, Kansans experiment (Businger et al. 1971).

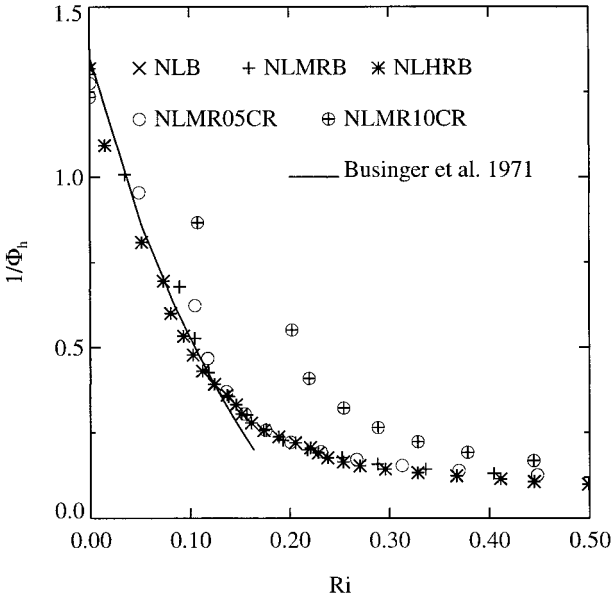


FIG. 4. Nondimensional potential temperature gradient as a function of the gradient Richardson number. Crosses, base cases NLMRB; pluses, medium-resolution base case NLMRB; stars, high-resolution base case NLHRB; circles, cooling rate 0.5 K $h^{-1}$, case NLMR05CR; crossed circles, cooling rate 1.0 K $h^{-1}$, case NLMR10CR; solid line, Kansans experiment (Businger et al. 1971).

sulting in unrealistically low TKE levels. The advantages of the nonlinear model are also demonstrated in Figs. 3 and 4. The nondimensional shear and the nondimensional mean potential temperature gradient are defined as

$$\Phi_m = \frac{\kappa z}{u_*}\left[\left(\frac{\partial U}{\partial z}\right)^2 + \left(\frac{\partial V}{\partial z}\right)^2\right]^{1/2}, \tag{27}$$

$$\Phi_h = \frac{\kappa z u_*}{q_*}\frac{\partial \Theta}{\partial z}. \tag{28}$$

Here, $u_*$ and $q_*$ are the surface friction velocity and the surface potential temperature flux; respectively. In Figs. 3 and 4, the nondimensional shear and the nondimensional potential temperature gradient are presented as a function of the local-gradient Richardson number, defined as

$$\mathrm{Ri} = \frac{\dfrac{g}{T_0}\dfrac{\partial \Theta}{\partial z}}{\left(\dfrac{\partial U}{\partial z}\right)^2 + \left(\dfrac{\partial V}{\partial z}\right)^2}. \tag{29}$$

We can conclude that for subcritical values of the gradient Richardson number, corresponding to the data points residing within the ABL, LES with the nonlinear model accurately reproduces observed (Businger et al. 1971) nondimensional shear and potential temperature gradient surface layer profiles. It has been shown by Andrén (1995) that LES with the linear, Smagorinsky-type model results in erroneous profiles.

For all of the LES cases, initial conditions, boundary conditions, and basic simulation parameters are summarized in Table 1. In the following sections, we will demonstrate that our choices of simulation parameters and initial and boundary conditions covered a wide parameter range, controlling the structure of a quasi-steady, stably stratified ABL.

## 5. Potential temperature and turbulence profiles and budgets

We define the ABL top as the level at which the tangential turbulent stress vanishes. We first determine the height at which tangential turbulent stress is reduced to 5% of its surface value, and then we linearly extrapolate to the level at which it would vanish if the stress profile was linear:

$$h = \frac{z(\langle uw\rangle = 0.05u_*^2)}{0.95}. \tag{30}$$

Here, angle brackets denote the average over horizontal planes. The flow is assumed to be horizontally homogeneous. A more detailed argument for our choice of the parameter that determines the ABL height, a description of mechanisms that control it, and a possible diagnostic equation for the stable ABL height will be presented in section 6.

Under the influence of surface cooling and the as-

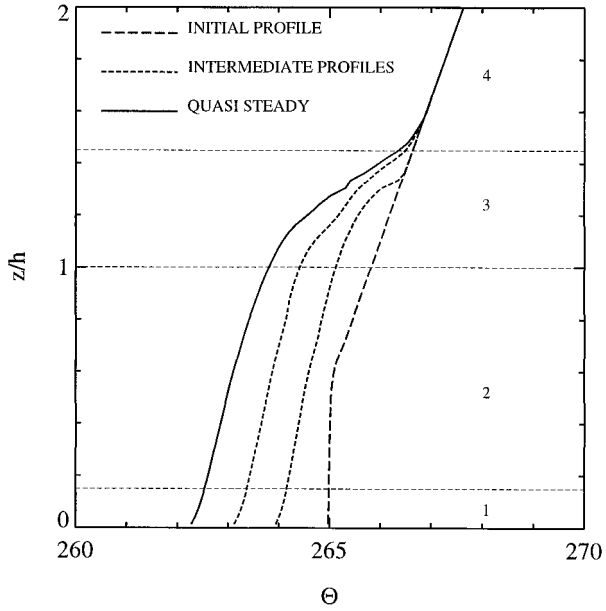


FIG. 5. The potential temperature profile evolution from LES NLHRB case. Solid line, the profile when quasi-steady state is reached after 12 h; dashed line, the initial profile; dotted line, intermediate profiles.

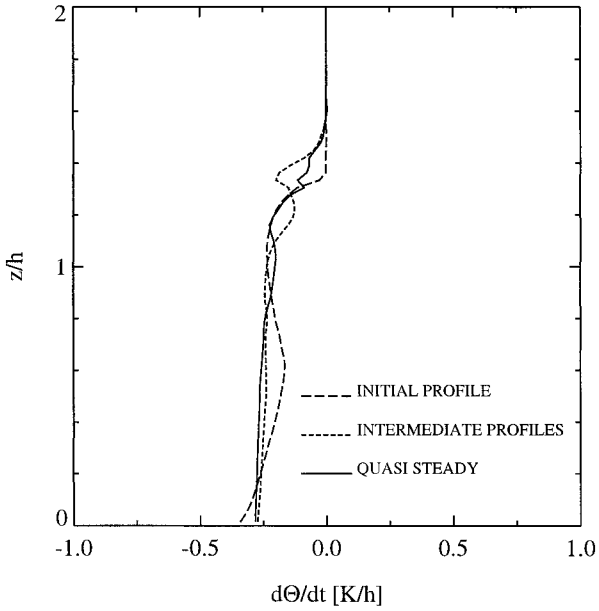


FIG. 6. Cooling rate profile evolution from LES NLHRB case. Solid line, the profile when quasi-steady state is reached; dashed line, the initial profile; dotted line, intermediate profiles.

sociated downward surface heat flux in LES of a stable ABL, we observe that the initially well-mixed layer develops an inversion first in the surface layer. If the surface cooling conditions are maintained long enough, due to the effects of turbulent mixing, a strong inversion develops at the top of the turbulent layer. From that point on, this second inversion determines the depth of the stable ABL. As the inversion strengthens, the buoyancy effects at the inversion suppress the turbulence production.

The structure of potential temperature profiles in a quasi-steady state indicates the existence of four layers (Fig. 5): 1) the surface layer, 2) the central layer where turbulence effects dominate, 3) the elevated inversion layer that caps the ABL, and 4) and the overlying inversion dominated by gravity waves. This structure was observed in a number of experiments (e.g., van Ulden and Wieringa 1996). The development of an elevated inversion was also a characteristic of second-order closure simulations (Delage 1974; Brost and Wyngaard 1978; Garratt and Brost 1981) and DNS (Coleman et al. 1992). However, the short integration time of only 2–3 h was not sufficient for the inversion to develop in previous LES of the stably stratified ABL (Mason and Derbyshire 1990; Brown et al. 1992; Andrén 1994).

We first analyze the simulated potential temperature and mean wind profiles of a quasi-steady, stably stratified ABL and compare them with the analytical model derived by Nieuwstadt (1985). Using the following assumptions, Nieuwstadt was able to obtain an analytical form of the quasi-steady state of a stably stratified ABL:

- turbulence is quasi stationary and horizontally homogeneous,
- there is a finite potential temperature jump at the top of a stable ABL,
- gradient and flux Richardson numbers are independent of height above the surface (local scaling), and
- a turbulent stress vector is aligned with the mean velocity gradient.

Derbyshire (1990) improved on Nieuwstadt's solution by matching surface-layer and outer-layer profiles. To obtain an even more realistic solution, Nieuwstadt's model should also include a correction of the potential temperature profile at the ABL top, since the assumed infinite temperature jump is unphysical. In reality, the temperature gradient at the ABL top increases, but only after a finite time remains finite. A strong temperature gradient at the ABL top is caused by turbulent mixing in the ABL and delineates the vertical level at which turbulence effects cease to dominate. In Fig. 5, the evolution of a potential temperature in a NLHRB case is presented. The dashed line represents the initial potential temperature profile, while the solid line represents a profile when a quasi-steady state is reached. Two intermediate potential temperature profiles are 4 and 8 h after the initialization of the simulation. Corresponding cooling-rate profiles are shown in Fig. 6. In a quasi-steady state, the cooling rate is constant throughout the ABL, and above the ABL top it smoothly approaches a zero value. From Fig. 5, we concluded that once the strong, elevated temperature inversion develops, it represents an ever-increasing obstacle to stable boundary

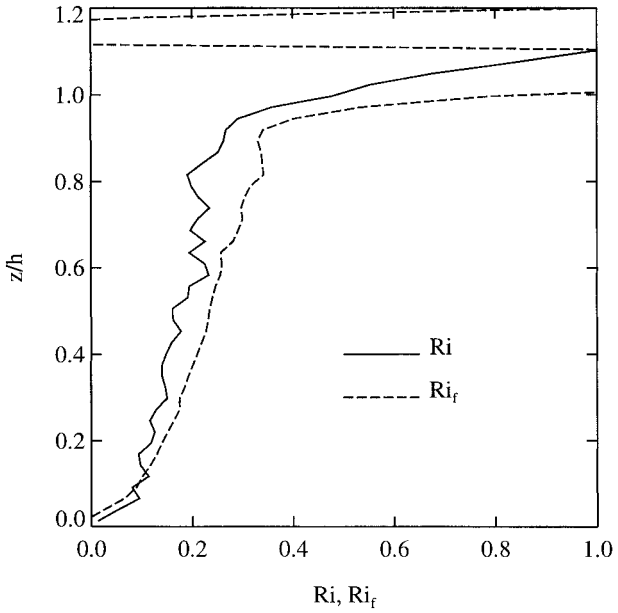


FIG. 7. Quasi-steady-state gradient and flux Richardson number profiles (NLHRB case). Solid line, gradient Richardson number; dashed line, flux Richardson number.

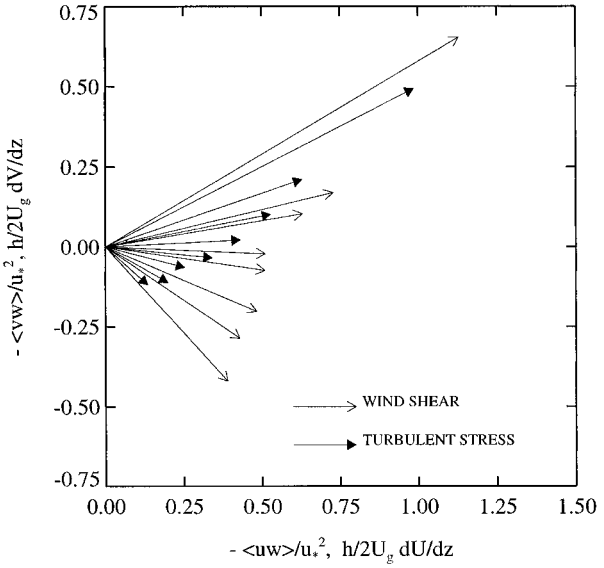


FIG. 8. Normalized shear, $h/(2U_g)(dU/dz\mathbf{i} + dV/dz\mathbf{j})$, and turbulent stress component: $1/u_*^2(\langle uw\rangle\mathbf{i} + \langle vw\rangle\mathbf{j})$; vectors (NLHRB case). Open arrows, shear vectors; full arrows, turbulent stress component vectors.

layer growth. We will demonstrate the importance of such an inversion on determining the ABL height.

In the outer layer of the ABL, both gradient and flux Richardson numbers (Fig. 7) vary slightly with height and appear to approach a constant value in a weakly stable case. It is obvious that the assumption that Richardson numbers are constant through the ABL is not a good approximation. This implies that a *z*-less stratification and local scaling hypothesis can be applied to a weakly stable case, but may not hold under stronger stability conditions. Notice that above the ABL top, both gradient and flux Richardson numbers increase sharply, and their critical value crossover point coincides with the ABL top defined by Eq. (30).

To test Nieuwstadt's assumption about alignment of wind shear vector and turbulent stress component vector, we plot both in Fig. 8. Commonly, the turbulent stress tensor is related to the mean strain rate tensor via a scalar eddy viscosity, which is obtained as a reduction of the second-order eddy viscosity tensor under the assumption of isotropy. From Fig. 8, it is obvious that such a scalar eddy viscosity is not a good approximation, and to express turbulent stresses as a function of the mean strain rate tensor, an anisotropic eddy viscosity tensor would have to be defined instead (Monin and Yaglom 1971).

The tangential turbulent stress and turbulent flux profiles are presented in Figs. 9 and 10. These profiles show that the tangential turbulent stress vanishes at levels lower than those of the turbulent flux. As a consequence of the vanishing of tangential stress, TKE production and dissipation vanish at the same level (Fig. 11). However, TKE itself vanishes at a higher level (Fig. 12). Normal turbulent stresses shown in Fig. 13 reveal that while the horizontal velocity variance is nonzero, the vertical velocity variance nearly vanishes, indicating a strong suppression of vertical motions within the elevated inversion. Furthermore, the TKE production and the dissipation vanish above the ABL top. Normal turbulent stress components, presented as a function of a local scaling parameter, $z/\Lambda$, where $\Lambda$ is the local Monin–Obukhov length scale, are shown in Fig. 14. In

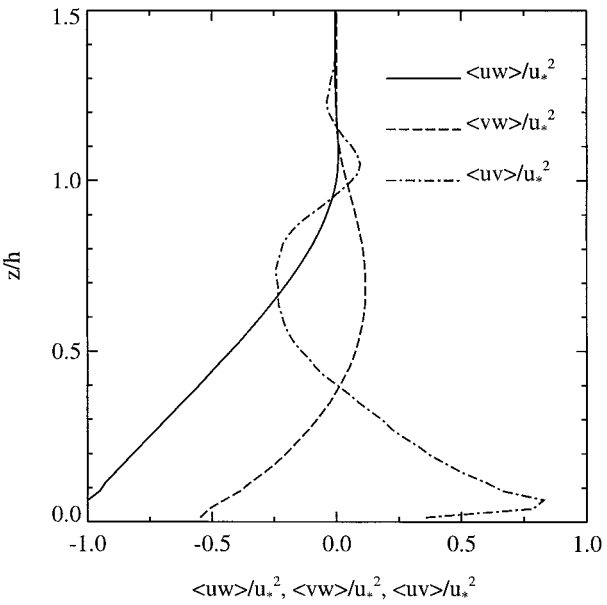


FIG. 9. Quasi-steady-state normalized tangential turbulent stress profiles (NLHRB case). Solid line, $\langle uw\rangle/u_*^2$; dashed line, $\langle vw\rangle/u_*^2$; dash–dot line, $\langle uv\rangle/u_*^2$.

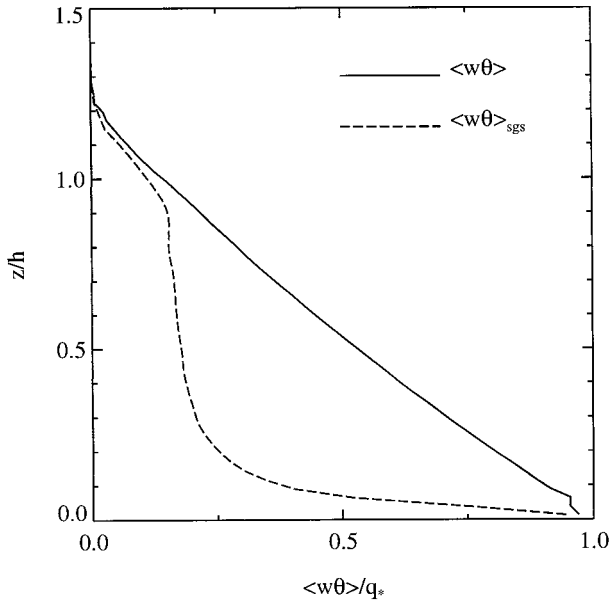


FIG. 10. Quasi-steady normalized potential temperature flux profiles (NLHRB case). Solid line, total potential temperature flux; dashed line, SGS potential temperature flux.

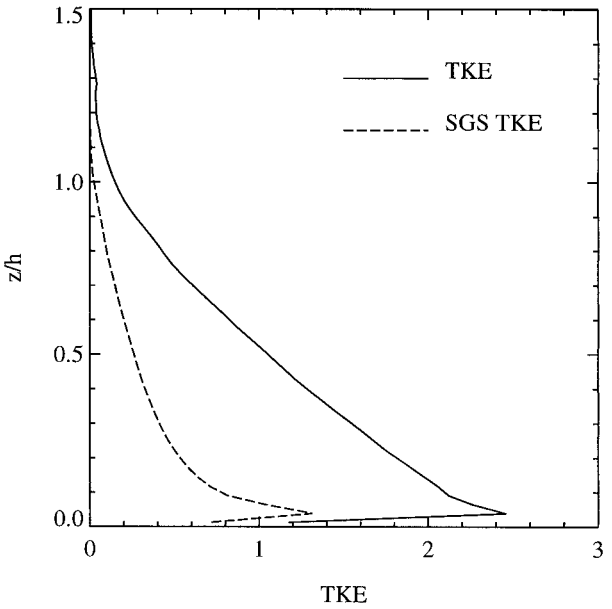


FIG. 12. Quasi-steady normalized TKE profiles (NLHRB case). Solid line, total TKE; dashed line, SGS TKE component.

accordance with Nieuwstadt's (1984) local scaling hypothesis, stress components approach constant values as the local scaling parameter increases. However, the surface-layer values of the nondimensional normal turbulent stresses are $\langle u^2\rangle/u_*^2 = 2.6$, $\langle v^2\rangle/u_*^2 = 1.9$ and $\langle w^2\rangle/u_*^2 = 0.9$ These values are lower than those reported by Nieuwstadt (1984, 1985): $\langle u^2\rangle/u_*^2 = 4.2$, $\langle v^2\rangle/u_*^2 = 3$ and $\langle w^2\rangle/u_*^2 = 1.9$ as a best fit through experimentally determined values. Spectra of the streamwise velocity and the vertical velocity at three different heights within the ABL and one above the ABL are presented in Figs. 15 and 16. Within the ABL, these spectra also scale according to the local scaling hypothesis (Sorbjan 1986).

While the structure of the ABL under weakly and moderately stable conditions is clearly dominated by

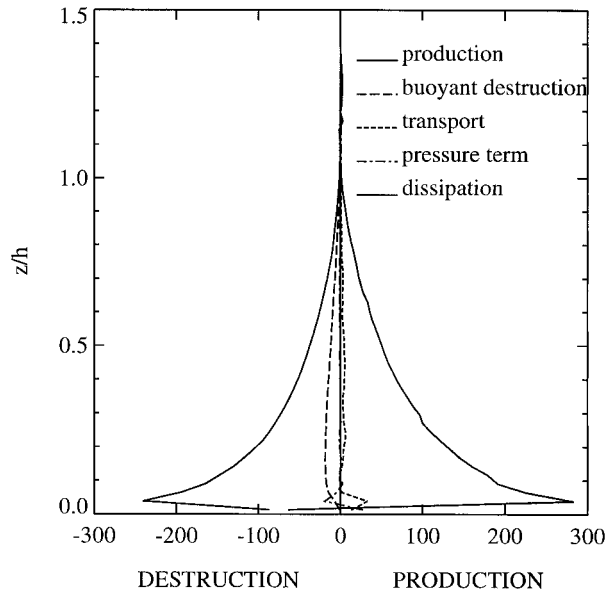


FIG. 11. TKE budget (NLHRB case). Solid lines, TKE production and TKE dissipation; dashed line, buoyant TKE destruction; dotted line, transport; dash–dot line, pressure term.

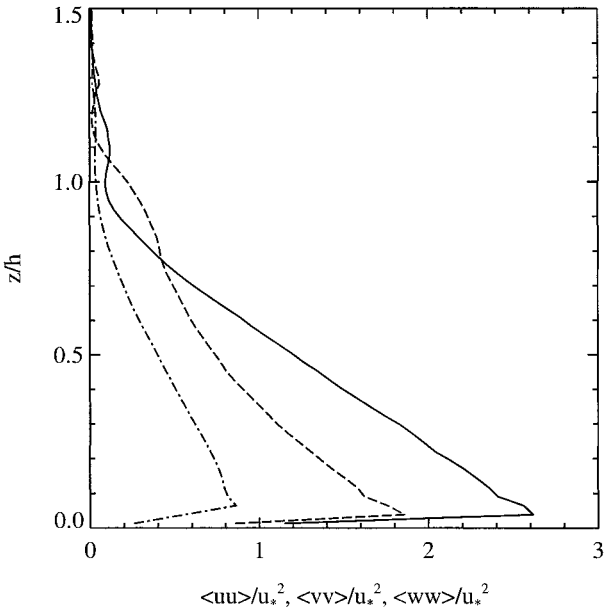


FIG. 13. Quasi-steady-state normal turbulent stress profiles (NLHRB case). Solid line, $\langle uu\rangle/u_*^2$; dashed line, $\langle vv\rangle/u_*^2$; dash–dot line, $\langle ww\rangle/u_*^2$.

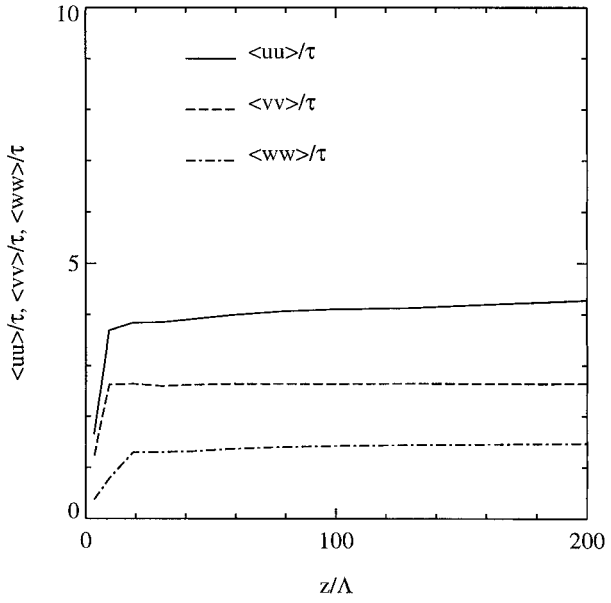


FIG. 14. Normal turbulent stress components scaled according to local scaling hypothesis and presented as a function of a local scaling parameter $z/\Lambda$ (NLHRB case). Here, $\tau = \tau(z)$ is a local turbulent stress value defined as $\tau = (\langle uw\rangle^2 + \langle vw\rangle^2)^{1/2}$. Solid line, $\langle uu\rangle/u_*^2$; dashed line, $\langle vv\rangle/u_*^2$; dash–dot line, $\langle ww\rangle/u_*^2$.

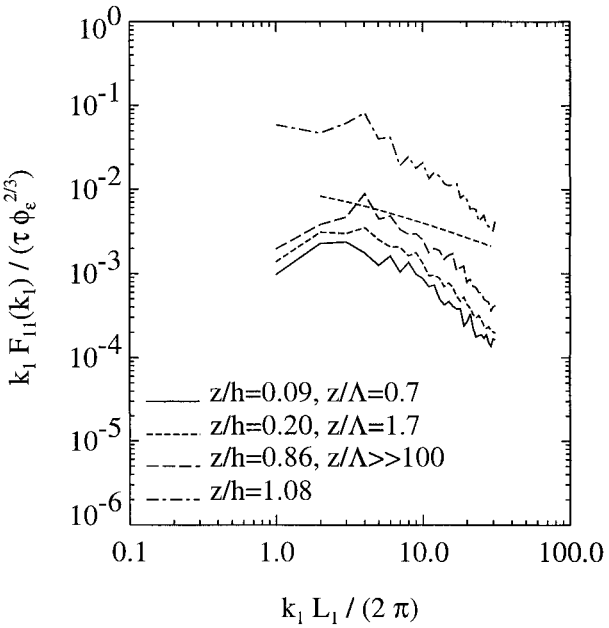


FIG. 15. Streamwise velocity spectra (NLHRB case). Solid line, $z/h = 0.09$, $z/\Lambda = 0.7$; dashed line, $z/h = 0.2$, $z/\Lambda = 1.7$; long-dash line, $z/h = 0.86$, $z/\Lambda \gg 100$; dash–dot line, $z/h = 1.06$.

turbulence effects, the structure of the elevated inversion cannot be easily discerned from LES results. The elevated inversion layer above the top of the ABL is characterized by strong vertical potential temperature gradient, shear caused by the presence of a jet, vanishing tangential turbulent stresses, strong suppression of vertical motions, and small but significant downward heat flux. From Fig. 7, we see that the gradient and the turbulence Richardson numbers are supercritical, and we can therefore conclude that the layer is not fully turbulent. Atmospheric observations by sodar (Neff 1986) as well as by LES of sheared, stratified homogeneous turbulence (Schumann 1996) suggest the presence of Kelvin–Helmholtz waves under such conditions. The resolution of our LES is not sufficient to resolve Kelvin–Helmholtz waves, but their signature is clearly present in mean and turbulence profiles as well as in turbulence budgets. Our LES results suggest that the wave motions in the elevated inversion support heat flux but not momentum flux.

An inversion wind maximum in the stably stratified ABL is often labeled low-level jet (LLJ). Observational evidence of existence of wind maxima within nocturnal inversions motivated Blackadar (1957) to analyze the effects of vanishing turbulent stresses at the top of an evolving stable ABL. He showed that geostrophic balance is disturbed under such conditions, and consequently the wind vector undergoes inertial oscillation. The period of the inertial oscillation is directly proportional to the Coriolis parameter and is thus longer at lower latitudes and shorter at high latitudes. Analyzing available observations, Blackadar also noticed that the wind speed maximum usually coincides with the top of the nocturnal inversion, and he suggested that it is a stable configuration.

Although low-level jets have been observed in a number of ABL experiments, in some cases there was more

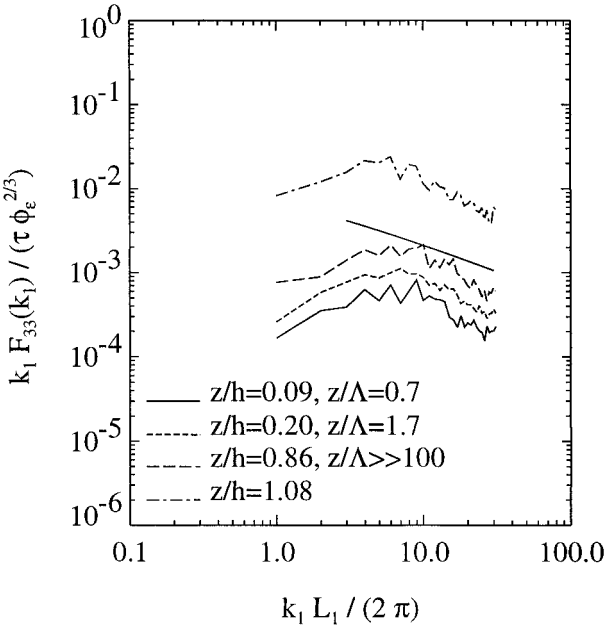


FIG. 16. Vertical velocity spectra (NLHRB case). Solid line, $z/h = 0.09$, $z/\Lambda = 0.7$; dashed line, $z/h = 0.2$, $z/\Lambda = 1.7$; long-dash line, $z/h = 0.86$, $z/\Lambda \gg 100$; dash–dot line, $z/h = 1.06$.

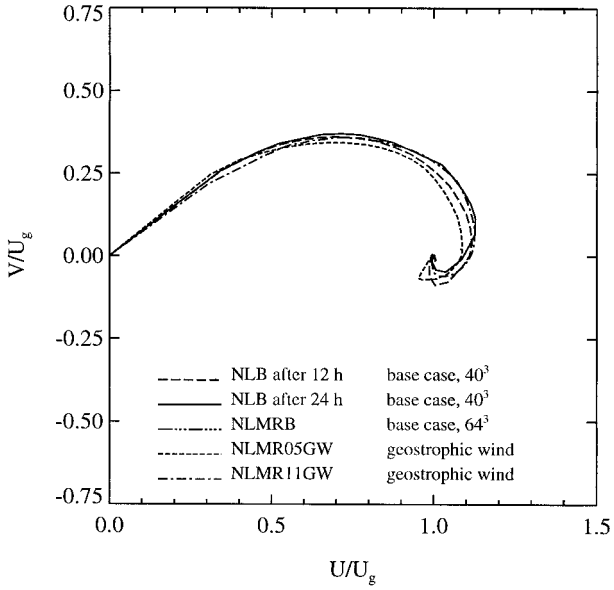


FIG. 17. Normalized Ekman spirals. Solid line, NLB case after 24 h; dashed line, NLB case after 12 h; dash–three-dots line, NLMRB case after 12 h; dotted line, NL05CR case after 12 h; dash–dot line, NL10CR case after 12 h.

than one mechanism contributing to development [such as inertial oscillation and large-scale sloping of the terrain in the Minnesota experiment; Caughey et al. (1979)]. However, for a few observations, we can be certain that only the inertial oscillation caused the development of the inversion wind maxima (Derbyshire 1995; van Ulden and Wieringa 1996; Pinto 1998).

In Fig. 17, we present Ekman spirals of quasi-steady wind profiles for the baseline LES case (NLB and NLMRB) as well as for the cases where we varied the geostrophic wind (NLMR05GW and NLMR11GW). It is obvious that in the outer layer, velocity (including the low-level jet) scales with the geostrophic wind speed as suggested by Nieuwstadt (1985). However, it should be pointed out that the angle between the low-level wind vector and the geostrophic wind vector is approximately 30°. This angle is much smaller than the angle of 60° that was predicted by Nieuwstadt's model.

Garratt (1992) argues that the within the ABL, the low-level jet results from a damped inertial oscillation due to the small but not vanishing turbulent stress. However, Nieuwstadt's (1984, 1985) simplified analytical model of a stable ABL produces a low-level jet as a quasi-steady feature. Our LES results indicate that the inversion wind maximum is indeed a feature of a quasi-steady state of a stably stratified ABL. Furthermore, LES results confirm Garratt's position, and we observe that the damping of the inversion wind maximum by the turbulent stress is relatively strong, so that only after one period it is sufficiently damped that the state can be considered quasi steady. This result is in agreement with the results obtained using a simple two-layer model developed by Thorpe and Guymer (1977). Turbulence near the ABL top is enhanced by the shear due to the low-level jet. The development of the wind maxima and its subsequent damping are therefore interdependent. The quasi-steady state is reached only when these two mechanisms—turbulence production due to the jet evolution and its damping by the turbulent stress—reach equilibrium. To test this, we carried out a simulation of the NLB case for 24 h of physical time and did not observe any significant changes in the ABL structure after 10 h of simulation, which approximately corresponds to one oscillation period at the given latitude of 73°N.

## 6. Boundary layer height

The height of the stable ABL represents an important length scale that is often combined with the Monin–Obukhov length scale to form a stability parameter, $\mu = h/L$. However, Zilitinkevich and Mironov (1996) pointed out that no expression for the equilibrium stable ABL height existed that would account for the combined effects of rotation, surface heat flux, and static stability in a free flow. They therefore proposed a new parameterization that includes all of these effects. We use their model and our LES results as a starting point in a search for a simple yet sufficiently accurate parameterization for the height of the stable ABL.

Before proceeding with analysis of boundary layer height parameterizations, we first consider different boundary layer height definitions presently in use. The stable ABL height is often defined as the height at which heat flux is reduced to some fraction (e.g., 5%) of its surface value (e.g., Caughey et al. 1979; Derbyshire 1990). Sometimes the stable ABL height is defined as the level at which the lowest wind maxima occurs (Malgarejo and Deardorff 1974) or the level to which the surface inversion extends (e.g., Yamada 1979). As mentioned earlier, we have adopted the definition based on the level at which the turbulent stress reduces to some fraction of its surface value (e.g., Businger and Arya 1974; Wyngaard 1975; Brost and Wyngaard 1978; Zilitinkevich and Mironov 1996). We argue that this definition is the most appropriate, since the height at which turbulent stress vanishes unequivocally defines the boundary between turbulent and nonturbulent layers. Vanishing heat flux does not clearly delineate turbulent layer boundary, since heat flux is often dominated by the effects of gravity waves near the stable ABL top. The evolution of the stable ABL height under different conditions is presented in Fig. 18. It is obvious that the ABL height is most significantly affected by the surface heat flux and by the geostrophic wind forcing.

While different prognostic equations have been proposed in the past for the evolution of ABL height toward the equilibrium height as a stably stratified ABL approaches a quasi-steady state (e.g., Zeman 1979; Nieuwsadt and Tennekes 1981; Mahrt 1981), we focus on determining the equilibrium height, since the knowl-

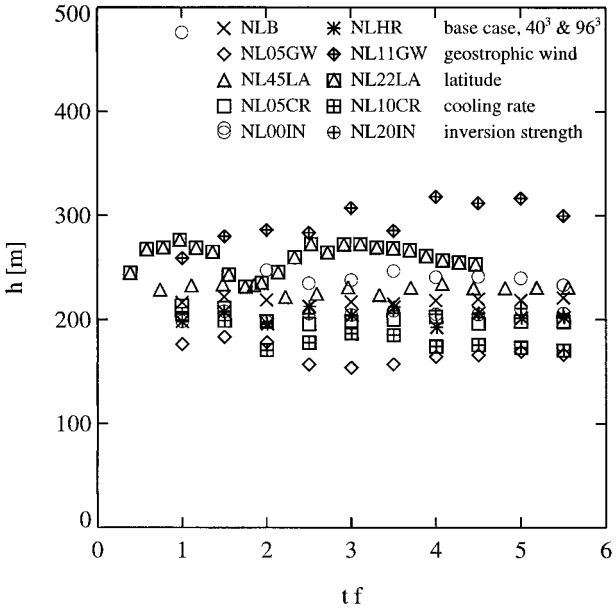


FIG. 18. Evolution of the boundary layer height for different initial and boundary conditions. Symbols represent 1-h averages. Crosses, base cases NLMRB; stars, high resolution base case NLHRB; diamonds, geostrophic wind 5 m $s^{-1}$, case NLMR05GW; crossed diamonds, geostrophic wind 11 m $s^{-1}$, case NLMR11GW; squares, latitude 45°N, case NLMR45LA; crossed squares, latitude 22°N, case NLMR22LA; triangles, cooling rate 0.5 K $h^{-1}$, case NLMR05CR; boxed triangles, cooling rate 1.0 K $h^{-1}$, case NLMR10CR; circles, inversion strengths 0.0 K $m^{-1}$, case NL00IN; crossed circles, inversion strengths 0.02 K $m^{-1}$, case NL20IN.

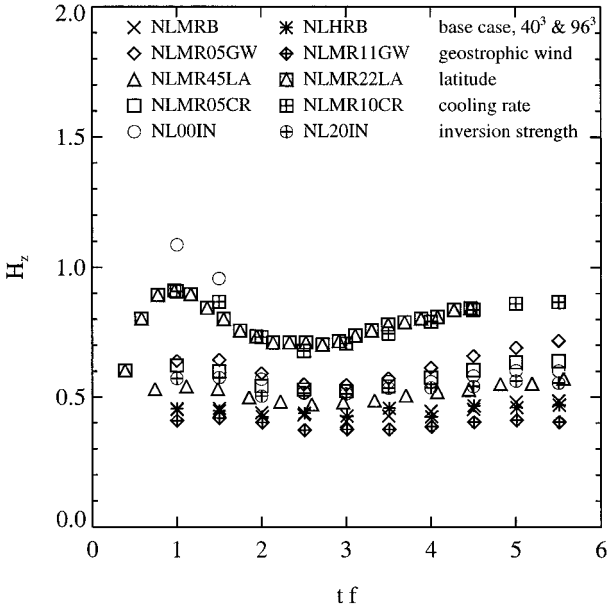


FIG. 19. Zilitinkevish–Mironov stable boundary layer height model with original model coefficients, normalized boundary layer height computed using LES results. Symbols represent 1-h averages. Crosses, base cases NLMRB; stars, high-resolution base case NLHRB; diamonds, geostrophic wind 5 m $s^{-1}$, case NLMR05GW; crossed diamonds, geostrophic wind 11 m $s^{-1}$, case NLMR11GW; squares, latitude 45°N, case NLMR45LA; crossed squares, latitude 22°N, case NLMR22LA; triangles, cooling rate 0.5 K $h^{-1}$, case NLMR05CR; boxed triangles, cooling rate 1.0 K $h^{-1}$, case NLMR10CR; circles, inversion strengths 0.0 K $m^{-1}$, case NL00IN; crossed circles, inversion strengths 0.02 K $m^{-1}$, case NL20IN.

edge of the equilibrium height is essential to determine the boundary layer growth-rate equation (Zilitinkevich and Mironov 1996).

Using the eddy viscosity concept, Zilitinkevich (1972) defined the depth of a turbulent, stably stratified ABL analogous to the Ekman layer depth to be $h = C_z(u_*L/f)^{1/2}$. Using the expression for the eddy-viscosity profile obtained from second-order closure simulations of Brost and Wyngaard (1978), Nieuwstadt (1980) modified the Zilitinkevich model and obtained a polynomial relation between two nondimensional parameters: the ratio of a boundary layer height to the Monin–Obukhov length scale and the Monin–Kazanski parameter. Kitagorodski and Joffre (1988) argued that the stable ABL height depends on the strength of the overlaying inversion, and they related the nondimensional parameter, $\mu$, to the nondimensional parameter including the Brunt–Väisälä frequency, $hu_*/N$. Recently, Zilitinkevich and Mironov (1996) proposed the following equilibrium height model based on the intermediate asymptotics:

$$\frac{h|f|^2}{C_n u_*} + \frac{h}{C_s L} + \frac{h|f|^{1/2}}{C_{sr}(u_* L)^{1/2}} + \frac{Nh}{C_i u_*} + \frac{h(N|f|)^{1/2}}{C_{ir} u_*^{1/2}} = 1. \quad (31)$$

Our LES results presented in Fig. 18 indicate that under commonly observed conditions, the strength of the overlying inversion has a negligible effect on the boundary layer height. Therefore, we consider only the first three terms of the left-hand side (LHS) of (34) and neglect the terms involving the Brunt–Väisälä frequency, $N$. In Fig. 19, the value of the LHS of (34) is computed using the results of LES and is presented as a function of the nondimensional time, $tf$. The model coefficients were set to the values suggested by Zilitinkevich and Mironov (1996), so that $C_n^2 = 1/4$, $C_s = 10$, and $C_{sr} = 1$. We should point out that each of these coefficients was determined independently using either experimental observations or numerical simulations.

Although our LES data and experimental evidence show that the Zilitinkevich–Mironov model (34) results in a large scatter and therefore cannot be considered as a suitable predictive tool for determining a stable ABL height, our simulations suggest that a more accurate model can be constructed using the same basic elements. To develop a more accurate model, we employ dimensional analysis. Notice that the first three terms on the LHS of (34) involve only four dimensional parameters: the boundary layer height, $h$; the Monin–Obukhov length, $L$; the surface friction velocity, $u_*$; and the Coriolis parameter, $f$. Dimensional analysis shows that by using these four parameters, we can form only two in-

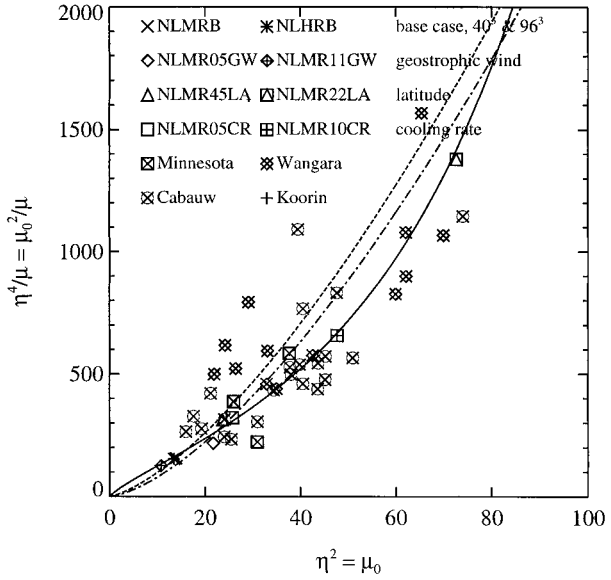


FIG. 20. Nondimensional parameter, $\mu_0^2/\mu(\mu = h/L)$, as a function of the Monin–Kazanski parameter, $\mu_0 = u_*/(fL)$. Crosses, base cases NLMRB; stars, high-resolution base case NLHRB; diamonds, geostrophic wind 5 m s$^{-1}$, case NLMR05GW; crossed diamonds, geostrophic wind 11 m s$^{-1}$, case NLMR11GW; squares, latitude 45°N, case NLMR45LA; crossed squares, latitude 22°N, case NLMR22LA; triangles, cooling rate 0.5 K h$^{-1}$, case NLMR05CR; boxed triangles, cooling rate 1.0 K h$^{-1}$, case NLMR10CR; circles, inversion strengths 0.0 K m$^{-1}$, case NL00IN; crossed circles, inversion strengths 0.02 K m$^{-1}$, case NL20IN.

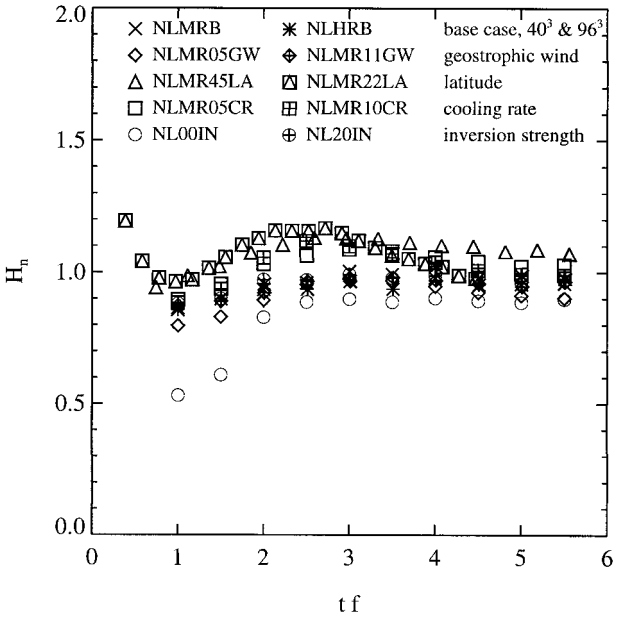


FIG. 21. Zilitinkevish–Mironov stable boundary layer height model with modified model coefficients computed as the least-squares fit to the LES results. Symbols represent one-hour averages. Crosses, base cases NLMRB; stars, high-resolution base case NLHRB; diamonds, geostrophic wind 5 m s$^{-1}$, case NLMR05GW; crossed diamonds, geostrophic wind 11 m s$^{-1}$, case NLMR11GW; squares, latitude 45°N, case NLMR45LA; crossed squares, latitude 22°N, case NLMR22LA; triangles, cooling rate 0.5 K h$^{-1}$, case NLMR05CR; boxed triangles, cooling rate 1.0 K h$^{-1}$, case NLMR10CR; circles, inversion strengths 0.0 K m$^{-1}$, case NL00IN; crossed circles, inversion strengths 0.02 K m$^{-1}$, case NL20IN.

dependent, nondimensional numbers. We choose the following nondimensional parameters: the stability parameter, $\mu = h/L$, and the Monin–Kazanski parameter, $\mu_0 = u_*/(|f|L) = \eta^2$. Alternatively, we could have chosen the nondimensional Ekman layer depth $d = (fh)/u_*$ and the stability parameter $\mu$, where the first parameter is the governing parameter in the neutral limit and the second is the governing parameter in the nonrotating flow limit.

Using LES data and experimental data from four experiments—Minnesota, Wangara, Koorin, and Cabauw (cf. Garratt 1982, appendix 2)—we proceed by searching for an implicit function, $F(\mu, \eta)$, that satisfies the equation $F(\mu, \eta) = 0$. We searched for an implicit function $F(\mu, \eta)$ that would provide the best, least squares fit to the LES results. This involved different combinations of parameter $\mu$ and its second power and parameter $\eta$ up to the power four. We found that the three terms from the truncated Zilitinkevich–Mironov model provided the optimal functional form, which resulted in a single-valued functional dependence between $\mu = f(\eta)$ within the given range of values of $\eta$. Recasting the Zilitinkevich–Mironov model in terms of parameters $\mu$ and $\eta$ results in an equation that is quadratic in $\mu$:

$$C_s\mu^2 + \left(C_n^2\eta^4 + \frac{C_n^2C_s}{C_{sr}}\eta^3\right)\mu - C_n^2C_s\eta^4 = 0. \quad (32)$$

The solution to this quadratic equation is

$$\mu = \frac{1}{2C_s}\left[-\left(C_n^2\eta^4 + \frac{C_n^2C_s}{C_{sr}}\eta^3\right) + \left(\left(C_n^4\eta^4 + \frac{C_n^2C_s}{C_{sr}}\eta^3\right)^2 + 4C_n^2C_s^2\eta^4\right)^{1/2}\right]. \quad (33)$$

The truncated Zilitinkevich–Mironov model results in the best fit to the numerical data when the model coefficients are set to $C_n^2 = 1/500$, $C_s = 2/3$, and $C_{sr} = -20/27$. Nieuwstadt (1980) showed that plotting the stability parameter $\mu$ as a function of the Monin–Kazanski parameter induces artificial quadratic dependence; therefore, as suggested by Nieuwstadt, we plot $\eta^4/\mu$ as a function of $\eta^2$ in Fig. 20. If the Monin–Obukhov length is known, the solution (33) provides an equation for the boundary layer height. Using new model coefficients and LES results, we plot the right-hand side of (31) in Fig. 21. We observe that as ABLs subjected to different stability conditions and forcing approach quasi-steady state, the truncated LHS of Eq. (31) aproaches a constant value of 1. This indicates that the Zilitinkevich–Mironov model with the new coefficients can be effectively used to determine the stable ABL height. For completeness, important boundary layer parameters discussed in this section are summarized in Table 3.

TABLE 3. Properties of simulated stable ABLs.

| Run | $u_*$ (m s$^{-1}$) | $q_*$ (m K s$^{-1}$) | $\alpha$ (°) | $h$ (m) | $L$ (m) |
|---|---|---|---|---|---|
| LB | 0.275 | −0.014 | 29.8 | 160 | 111 |
| AB | 0.312 | −0.017 | 26.4 | 212 | 133 |
| NLB | 0.325 | −0.019 | 26.9 | 221 | 137 |
| NL45LA | 0.292 | −0.019 | 28.9 | 231 | 97 |
| NL22LA | 0.238 | −0.022 | 31.8 | 253 | 47 |
| NL05GW | 0.223 | −0.014 | 24.4 | 166 | 62 |
| NL11GW | 0.443 | −0.023 | 25.6 | 300 | 283 |
| NL05CR | 0.313 | −0.029 | 27.0 | 198 | 81 |
| NL10CR | 0.303 | −0.048 | 27.8 | 170 | 45 |
| NL00IN | 0.326 | −0.018 | 26.5 | 233 | 145 |
| NL20IN | 0.324 | −0.019 | 26.3 | 206 | 134 |
| NL05SR | 0.311 | −0.018 | 24.1 | 216 | 126 |
| NL20SR | 0.341 | −0.020 | 29.6 | 226 | 153 |
| NLMRB | 0.318 | −0.015 | 29.0 | 203 | 165 |
| NLMR45LA | 0.281 | −0.015 | 32.7 | 207 | 115 |
| NLMR22LA | 0.224 | −0.015 | 36.7 | 219 | 57 |
| NLMR05GW | 0.209 | −0.010 | 29.3 | 149 | 69 |
| NLMR11GW | 0.459 | −0.023 | 28.5 | 286 | 321 |
| NLMR05CR | 0.295 | −0.024 | 31.6 | 170 | 82 |
| NLMR10CR | 0.282 | −0.040 | 33.0 | 147 | 43 |
| NLHR | 0.321 | −0.015 | 28.5 | 202 | 172 |

## 7. Summary

We have studied the evolution of a stably stratified ABL toward a quasi-steady state using LES. We used BASE data to impose initial and boundary conditions. We performed LESs of a homogeneous, clear-air Arctic boundary layer, characterized by a weak to moderate downward heat flux at the surface, moderate to strong geostrophic winds, and an overlaying inversion. We observed a general agreement between observations or theoretical models and LES results.

Using LES, we examined stably stratified boundary layers under different conditions for a long period of time so that the inertial oscillation was sufficiently damped with a sufficiently high resolution to resolve energy containing eddies. We have shown that under the assumption of horizontal homogeneity and negligible mesoscale effects, an ABL subjected to negative surface heat flux can reach a quasi-steady state. In our LES, the quasi-steady state is reached after a period of time proportional to the period of the damped inertial oscillation that an ABL undergoes when the turbulent stress at the ABL top vanishes. We used the results of low-resolution LES to calculate the bulk properties of stable ABLs as they evolve under different initial and boundary conditions and compared them with the experimental observations. Using the high-resolution simulation results only, we computed mean and turbulence profiles and turbulence budgets. Our simulations replicated the two-layer structure of the ABL, consisting of the surface layer dominated by surface fluxes and stresses and the outer layer dominated by turbulence effects. Above the ABL, we could also distinguish two layers: an elevated inversion the strength of which increases with time and an overlaying constant strength inversion above it, which was dominated by gravity waves.

A comparison with Nieuwstadt's analytical stable ABL model showed a good agreement despite the fact that none of the assumptions used to derive the model was strictly satisfied. This supports Derbyshire's conclusion that the extended Nieuwstadt model provides a simple yet useful framework for a study of the quasi-steady, stably, stratified ABLs. Our LES results confirmed Nieuwstadt's argument that the velocity profile above the surface layer, particularly the low-level jet, scales with the geostrophic wind.

One of the most important ABL parameters is the boundary layer height. We defined the stable boundary layer height as the height at which tangential turbulent stress vanishes or, equivalently, the level at which turbulent production vanishes. Our results suggest that several different definitions of a stable boundary layer height can be considered equivalent, since the level at which tangential turbulent stresses vanish coincides with the low-level jet and with the level at which both gradient and flux Richardson numbers become supercritical. In contrast to that, LES results indicate that although commonly used, the level at which heat flux vanishes would not be appropriate boundary layer height.

Although turbulence reaches equilibrium relatively quickly, within a few hours after the transition, important flow parameters such as a bulk Richardson number, boundary layer height, and low-level jet approach a steady state only at a much later stage after approximately one period of the damped inertial oscillation. In this sense, Hunt's (1985) statement that the structure of the stable ABL is probably too variable to be characterized reliably by typical profiles of the turbulence and mean velocity represents an accurate assessment of the stable ABL modeling problem. We therefore conclude that the LES results presented here cannot be validated in detail by comparison with midlatitude experimental observations. Experiments conducted at high latitude are therefore essential for obtaining a better insight into the structure of a quasi-steady, stably stratified ABL. Such observations are essential to develop a definitive theoretical framework for evolution of stably stratified ABL, since a quasi-steady state represents a long time limit of the evolution of stable ABLs. The Surface Heat Budget of the Arctic Ocean (SHEBA) experiment should provide necessary observations and information to form such a framework for quasi-steady, stably stratified ABLs.

*Acknowledgments.* This work was supported by a grant from NASA FIRE and, in part, by a grant of HPC time from the Arctic Region Supercomputing Center.

## REFERENCES


Andreas, E. L, 1996: *The Atmospheric Boundary Layer Over Polar Marine Surfaces. U.S. Army Cold Regions Research and Engineering Laboratory Monogr. No. 96-2,* 38 pp.

Andrén, A., 1995: The structure of stably stratified atmospheric boundary layers: A large-eddy simulation study. *Quart. J. Roy. Meteor. Soc.,* **121,** 961–985.

Blackadar, A. K., 1957: Boundary layer wind maxima and their significance for the growth of nocturnal inversions. *Bull. Amer. Meteor. Soc.,* **38,** 283–290.

Brost, R. A., and J. C. Wyngaard, 1978: A model study of the stably stratified planetary boundary layer. *J. Atmos. Sci.,* **35,** 1427–1440.

Brown, A., S. H. Derbyshire, and P. J. Mason, 1994: Large-eddy simulation of stable atmospheric boundary layers with a revised stochastic subgrid model. *Quart. J. Roy. Meteor. Soc.,* **120,** 1485–1512.

Businger, J. A., and S. P. S. Arya, 1974: Height of the mixed layer in the stably stratified planetary boundary layer. *Advances in Geophysics,* Vol. 18A, Academic Press, 127–158.

——, J. C. Wyngaard, Y. Izumi, and E. F. Bradley, 1971: Flux–profile relationships in the atmospheric surface layer. *J. Atmos. Sci.,* **28,** 181–189.

Canuto, V. M., and Y. Cheng, 1997: Determination of the Smagorinsky–Lilly constant $C_s$. *Phys. Fluids,* **9,** 1368–1378.

Caughey, S. J., J. C. Wyngaard, and J. C. Kaimal, 1979: Turbulence in the evolving stable boundary layer. *J. Atmos. Sci.,* **36,** 1041–1052.

Coleman, G. N., J. H. Ferziger, and P. R. Spalart, 1992: Direct simulation of the stably stratified turbulent Ekman layer. *J. Fluid Mech.,* **244,** 677–712.

Curry, J. A., W. B. Rossow, D. Randall, and J. L. Schramm, 1996: Overview of Arctic cloud and radiation characteristics. *J. Climate,* **9,** 1731–1764.

Deardorff, J. W., 1980: Stratocumulus-capped mixed layers derived from a three-dimensional model. *Bound.-Layer Meteor.,* **18,** 495–527.

Delage, Y., 1974: A numerical study of the nocturnal atmospheric boundary layer. *Quart. J. Roy. Meteor. Soc.,* **100,** 351–364.

Derbyshire, S. H., 1990: Nieuwstadt's stable boundary layer revisited. *Quart. J. Roy. Meteor. Soc.,* **116,** 127–158.

——, 1994: A ''balanced'' approach to stable boundary layer dynamics. *J. Atmos. Sci.,* **51,** 3486–3504.

——, 1995: Stable boundary layers: Observations, models and variability. Part I: Modelling and measurements. *Bound.-Layer Meteor.,* **74,** 19–54.

Garratt, J. R., 1992: *The Atmospheric Boundary Layer.* Cambridge University Press, 316 pp.

——, and R. A. Brost, 1981: Radiative cooling effects within and above the nocturnal boundary layer. *J. Atmos. Sci.,* **38,** 2730–2746.

Hunt, J. C. R., 1985: Diffusion in the stably stratified atmospherica boundary layer. *J. Climate Appl. Meteor.,* **24,** 1187–1195.

——, J. C. Kaimal, and J. E. Gaynor, 1985: Some observations of turbulence structure in stable layers. *Quart. J. Roy. Meteor. Soc.,* **111,** 793–815.

——, D. D. Stretch, and R. E. Britter, 1988: Length scales in stabley stratified turbulent flows and their use in turbulence models. *Stably Stratified Flow and Dense Gas Dispersion,* J. S. Puttok, Ed., Clarendon Press, 285–321.

——, G. J. Shutts, and S. H. Derbyshire, 1996: Stably stratified flows in meteorology. *Dyn. Atmos. Oceans,* **23,** 63–79.

Kim, J., and L. Mahrt, 1992: Simple formulation of turbulent mixing in the stable free atmosphere and nocturnal boundary layer. *Tellus,* **44A,** 381–394.

Kitagorodskii, S. A., and S. M. Joffre, 1988: In search of a simple scaling for the height of the stratified atmospheric boundary layer. *Tellus,* **40A,** 419–433.

Klemp, J. B., and D. R. Duran, 1983: An upper boundary condition permitting internal gravity wave radiation in numerical mesoscale models. *Mon. Wea. Rev.,* **111,** 430–444.

Kosović, B., 1997: Subgrid-scale modelling for the large-eddy simulation of high-Reynolds-number boundary layers. *J. Fluid Mech.,* **336,** 151–182.

Lilly, D. K., 1967: The representation of small-scale turbulence in numerical experiment. *Proc. IBM Scientific Computing Symp. on Environmental Sciences,* White Plains, NY, IBM, 195–210.

Mahrt, L., 1981: Modelling the depth of the stable boundary-layer. *Bound.-Layer Meteor.,* **21,** 3–19.

——, 1989: Intermittency of atmospheric turbulence. *J. Atmos. Sci.,* **46,** 79–95.

Malgarejo, J. W., and J. W. Deardorff, 1974: Stability functions for the boundary layer resistance laws based upon observed boundary layer heights. *J. Atmos. Sci.,* **31,** 1324–1333.

Mason, P. J., and D. J. Derbyshire, 1990: Large-eddy simulation of the stably stratified atmospheric boundary layer. *Bound.-Layer Meteor.,* **53,** 117–162.

——, and D. J. Thomson, 1992: Stochastic backscatter in large-eddy simulations of boundary layers. *J. Fluid Mech.,* **242,** 51–78.

Moeng, C.-H., 1984: A large-eddy-simulation model for the study of planetary boundary layer turbulence. *J. Atmos. Sci.,* **41,** 2052–2062.

Monin, A. S., and A. M. Yaglom, 1971: *Statistical Fluid Mechanics: Mechanics of Turbulence.* Vol. 1. The MIT Press, 769 pp.

Neff, W. D., 1986: Acoustic remote sensing. *Probing the Atmospheric Boundary Layer,* D. H. Lenschow, Ed., Amer. Meteor. Soc., 201–239.

Nieuwstadt, F. T. M., 1980: The steady-state height and resistance laws of the nocturnal boundary layer: Theory compared with Cabauw observations. *Bound.-Layer Meteor.,* **20,** 3–17.

——, 1984: The turbulent structure of the stable, nocturnal boundary layer. *J. Atmos. Sci.,* **41,** 2202–2216.

——, 1985: A model for the stationary, stable boundary layer. *Turbulence and Diffusion in Stable Environments,* J. C. R. Hunt, Ed., Clarendon Press, 149–179.

——, and H. Tennekes, 1981: A rate equation for the nocturnal boundary-layer height. *J. Atmos. Sci.,* **38,** 1418–1428.

Pinto, J. O., 1998: Autumnal mixed-phase cloudy boundary layers in the Arctic. *J. Atmos. Sci.,* **55,** 2016–2038.

Schumann, U., 1991: Subgrid length-scales for large-eddy simulation of stratified turbulence. *Theor. Comput. Fluid Dyn.,* **2,** 279–290.

——, 1996: Direct and large eddy simulations of stratified homogeneous shear flows. *Dyn. Atmos. Oceans,* **23,** 81–98.

Sorbjan, Z., 1986: Local similarity of spectral and cospectral characteristics in the stable-continuous boundary layer. *Bound.-Layer Meteor.,* **35,** 257–275.

Sullivan, P. P., J. C. McWilliams, and C.-H. Moeng, 1994: A subgrid-scale model for large-eddy simulation of planetary boundary-layer flows. *Bound.-Layer Meteor.,* **71,** 247–276.

Thorpe, A. J., and T. H. Guymer, 1977: The nocturnal jet. *Quart. J. Roy. Meteor. Soc.,* **103,** 633–653.

van Ulden, A. P., and J. Wieringa, 1996: Atmospheric boundary layer research at Cabauw. *Bound.-Layer Meteor.,* **78,** 39–69.

Wyngaard, J. C., 1975: Modeling the planetary boundary layer—Extension to the stable case. *Bound.-Layer Meteor.,* **9,** 441–460.

——, and B. Kosovic, 1994: Similarity of structure-function parameters in the stably stratified boundary layer. *Bound.-Layer Meteor.,* **71,** 277–296.

Yamada, T., 1979: Prediction of the nocturnal surface inversion height. *J. Appl. Meteor.,* **18,** 526–531.

Zeman, O., 1979: Parameterization of the dynamics of stable boundary layers and nocturnal jets. *J. Atmos. Sci.,* **36,** 792–804.

Zilitinkevich, S. S., 1972: On the determination of the height of the Ekman boundary layer. *Bound.-Layer Meteor.,* **3,** 141–145.

——, and D. V. Mironov, 1996: A multi-limit formula for the equilibrium depth of a stably stratified boundary layer. *Bound.-Layer Meteor.,* **3,** 325–351.